Sensitivity Improvement of a silicon waveguide Mach-Zehnder interferometer sensor decorated with olfactory receptors

Hibiki Watanabe [1*†], Masahiko Hasumi [1†], Yutaka Kuwamura [2,3†], Yosuke Fukutani [2,3†], and Hiromasa Shimizu [1*, **†]

Tokyo University of Agriculture and Technology, Koganei, Tokyo, 184-8588, Japan Departments of Applied Physics and Chemical Engineering[1], Biotechnology and Life Science[2], and Advanced Interdisciplinary Science[3]

*E-mail: s248232r@st.go.tuat.ac.jp; h-shmz@cc.tuat.ac.jp

**Corresponding author

[†]H. S. and Y. F. designed the project. H. W., M. H., and H. S. fabricated, and characterized the sensor devices. Y. K. and Y. F. performed the synthesis of ND-ORs and characterization by ELIZA method. H. W. Y. F. and H. S. wrote the paper.

We characterized the response of the olfactory receptor (OR) OR51E2 to the target molecule sodium acetate using silicon Mach–Zehnder interferometer (MZI) sensors. Successful immobilization of the ORs on the Si surface was confirmed. The sensor exhibited reversible responses, with a sensitivity enhancement of 3.1-fold compared to a reference MZI sensor without ORs at a concentration of 1×10^{-3} mol/L. A substantial local refractive index change, estimated to be as high as 3.1×10^{-3} RIU, was derived from the experimental signals, demonstrating the potential of olfactory sensing based on silicon photonic technologies.

Olfactory sensors capable of quantifying various smells are needed in a wide range of fields including health care, security, food inspection, cosmetics, and environmental monitoring [1-7]. Olfactory receptors (ORs) in animals serve as molecular recognition elements and offer high sensitivity and selectivity for detecting odorant molecules [8, 9]. Cadaverine detection has been demonstrated using a nanodisc-based bioelectronic nose with carbon nanotube transistors and TAAR13c-enbedded nanodiscs [10]. Octenol detection has been achieved using insect ORs (OR-Orco) forming a ligand-gated ion channel reconstructed into a lipid bilayer. [11]. Specific detection of nonanoic acid was reported with graphene-based field-effect transistors (FETs) decorated with cOR52 [12]. However, no studies have reported photonic sensors using ORs, that can detect the refractive index (RI) change by molecular recognition of ORs through evanescent wave near dielectric/semiconductor waveguides. Evanescent wave-based detection enables weak and reversible interactions with odorant molecules, compared with the sensors based on FET. Approximately 400 and 800 functional ORs have been identified in the genome DNA sequence of humans and dogs, respectively. Si photonic olfactory sensors offer large scale integration with diverse ORs from variant organisms, enabling the development of electronic nose. In this study, we report on a Si Mach Zehnder interferometer (MZI) sensors functionalized with OR51E2, which responds to acetic acid [9], and 3.1-fold improvement in sodium acetate (SA) sensitivity under wet conditions.

Ring resonators and MZIs have been used as RI sensors based on Si photonics. Since RI changes caused by odorant low molecular compounds are smaller than those from macromolecules like antigens in biosensor [13-16], higher sensitivity is needed. MZI sensitivity depends on the length of the sensing region interacting with molecules, and can be enhanced by extending the sensing region. Therefore, we chose MZI sensors for their expected higher sensitivity [17-21]. Figure 1 shows the schematic image of the MZI sensors decorated with ORs. The output light intensity I_{out} depends on the phase difference $\Delta\phi$ between the two waveguide arms of the MZI sensors, and is given by Eqs. (1), and (2).

$$I_{out} \propto \frac{1}{2}[1 + Vcos(\Delta\phi)] \quad (1)$$

$$\Delta\phi = \frac{2\pi}{\lambda}\{n_1 L_1 - (n_1 L_2 + n_s L)\} \quad (2)$$

,where V is the visibility of the interferometer determined by the propagation loss difference between the arms, n_s and n_1 are the effective refractive index of the sensing and reference waveguide respectively, L, L_1 and L_2 denote the length of the sensing waveguide, reference waveguide, the lower waveguide with the protective layer (excluding L), and λ is the wavelength. A 2x3 multimode interference (MMI) waveguide was used for interference of

the propagating light from the two arms to detect the phase shift caused by adsorption and desorption of odorant molecules [17]. The output light intensities for three output waveguides and recovered phase shifts $\Delta\phi$ are expressed as Eq. (3), and (4).

$$I_{out,i} \propto \frac{1}{2}\left[1 + Vcos\left\{\Delta\phi + \frac{2}{3}\pi(i-1)\right\}\right],\ (i = 1,2,3) \quad (3)$$

$$\Delta\phi = \arctan\{\frac{I_{out,2} - \frac{1}{2}I_{out,1} - \frac{1}{2}I_{out,3}}{\frac{\sqrt{3}}{2}(I_{out,3} - I_{out,1})}\} \quad (4)$$

The cross-sections of the Si waveguides for the reference and sensing regions are shown in Fig. 2. Transverse magnetic (TM) mode light of a wavelength of 1300 nm was used as input. TM mode provides stronger evanescent field distribution at the sensing region than transverse electric (TE) mode. The waveguide width *w* and height *h* were fixed at 600 and 250 nm, respectively. A SiO_2 protective layer was deposited over the reference and input/output waveguides, including the MMI splitter and combiner, to suppress the interference from odorant molecules in saline. Since ORs operate in aqueous environments, such as lipid membranes covered by mucus in olfactory epithelium, saline was assumed to cover all waveguides. The sensing region length *L* was set to 1.4 mm. Si MZI waveguides were fabricated on a silicon-on-insulator substrate using electron-beam lithography and reactive ion etching. A 300 nm-thick SiO_2 layer was deposited over the substrate excluding the sensing region by RF magnetron sputtering and lift-off. Fig. 2 shows an optical microscope image of the fabricated devices.

Synthesis and immobilization of ORs were performed as follows. To facilitate immobilization onto a Si substrate, a single cysteine residue was artificially added to the C-terminus of each OR. Plasmid DNA constructs were generated by individually inserting Olfr1377-Cys(OR1377), Olfr1484-Cys(OR1484) [22], OR51E2-Cys, and the nanodisc scaffold protein His-spMSP1D1 into pEU vectors. The OR1377 and OR1484 respond to the aromatic compound acetophenone ($C_6H_4COCH_3$), whereas OR51E2 responds to the linear fatty acids acetic acid (CH_3COOH) and propionic acid (CH_3CH_2COOH). Each OR was also fused at its N-terminus with a streptavidin-binding peptide (SBP-tag) and an HA-tag to facilitate purification and confirm immobilization following cell-free protein synthesis. Based on these plasmids, nanodisc-embedded ORs (ND-ORs), whose diameter is about 10 nm, were synthesized using the NanoDisc BD Kit (Cell Free Science), according to the manufacturer's protocol [23]. During the protein translation reaction, mRNAs encoding each OR and the scaffold protein were co-translated in a wheat germ cell-free expression system,

allowing for the simultaneous synthesis of ORs and their incorporation into nanodiscs. Following synthesis, the reaction mixture was applied to a Streptavidin Sepharose column (Cytiva), which binds the SBP-tag on the ORs. ND-ORs were subsequently purified via affinity chromatography using d-desthiobiotin as a competitive elution agent. ND-ORs was immobilized on the Si MZI sensor using the following procedure. Cleaved dies (7 mm x 10 mm) were heated at 250 ºC for 5 min. under ozone atmosphere. Silanization with amino bases was then performed in ethanol containing 2 vol.% of 3-Aminopropyltriethoxysilane (APTES, TOKYO CHEMICAL INDUSTRY, A0439) under nitrogen atmosphere. After 1 hour of incubation, the dies were rinsed three times with ethanol and deionized water and then dried under dry air, followed by annealing at 150 ºC for 30 min. Maleimide bases were introduced to bind specifically with the cysteine residue of ND-ORs on the silanized surface by incubating the dies in $1.2x10^{-3}$ mol/L solution of N-(6-Maleimidocaproyloxy) sulfosuccinimide sodium salt (sulfo-EMCS, Dojindo Molecular Technologies, S024) in deionized water solution. After 1 hour of incubation at room temperature, the dies were rinsed with deionized water and dried. PDMS (polydimethylpolysiloxane) μ-fluidic with input/output ports and an inner space of 3 mm x 1 mm x 5 mm was placed on the dies and tubes with (0.75 mm diamter) were connected. A 20 μL solution of the ND-ORs (0.03 mg/mL) was introduced by a syringe. The tubes were sealed with two parafilm sheets to prevent the ND-ORs from drying, and stored at 5ºC overnight for immobilization and incubation. Then 100 μL of HEPES (4-(2-Hydroxyethyl) piperazine-1-ethanesulfonic acid)) buffer (0.05 mol/L) was injected into the PDMS μ-fluidic for rinsing. To confirm the immobilization of ND-ORs on the Si surface, we evaluated their surface density using an ELISA (enzyme-linked immunosorbent assay) approach. The Si substrate was functionalized with maleimide groups with the same protocol. In this ELISA assay, enzyme-labeled ND-ORs were detected using an anti-HA antibody conjugated to horseradish peroxidase (HRP). Upon reaction with the substrate EzELISA TMB (ATTO) [24], changes in optical absorbance at the 450 nm wavelength light were measured to quantify ND-ORs binding. Figure 3 shows the absorbance at concentrations of 0.03, 0.1, and 0.3 mg/mL for OR1377 and OR1484. Absorbance without ND-ORs was measured as a reference. Immobilization characteristics of OR1377/1484 were essentially the same as those of OR51E2 used later for SA response measurements, despite the difference in OR type. Increased absorbance upon adding OR1377/1484 indicates successful immobilization on the Si surface. The absorbances for all the concentrations were almost the same, indicating that 0.03 mg/mL is sufficient for immobilization, therefore this

concentration was used for OR51E2 throughout the study.

The die with the PDMS μ-fluidic was mounted on the optical stage. TM mode light with a wavelength of 1300 nm and an intensity of 4 mW was input by a lensed optical fiber from a wavelength tunable laser and a polarization controller. Output from 3 output waveguides was detected with an infrared camera (Micron viewer 7290A, Spectra-physics) with a x20 objective lens, and their luminance was recorded as the output light intensities. First, we measured the fiber-coupled light intensity of the die without OR51E2 decoration in air, by changing the wavelength from 1298 to 1302 nm. The output phases differed by $2\pi/3$ and $4\pi/3$, as shown in Fig. 4(a)showing that MZI with three output waveguides operated properly.

The time transition of the responses by injecting the odorant molecules at the fixed wavelength of 1300 nm was obtained by the recovered phase shifts $\Delta\phi$ based on Eq.(4)Sodium acetate (CH_3COONa) solutions (0.1, 0.5, 1, and $5x10^{-3}$ mol/L) diluted with 0.05 mol/L HEPES were used as the odorant molecules in this study, in terms of neutral pH avoiding the influences by hydrogen ions in acetic acid (CH_3COOH). The flow rates from a syringe pump were kept constant at 0.1 mL/min. The solutions of each concentration were supplied for 150 sec. followed by 0.05 mol/L HEPES buffer for refreshing the surface.

Figures 4(b) and (c) show the recovered phase shift at 0.25-second intervals upon SA injections with and without OR51E2. The phase shifts increased after the SA injection and returned upon switching to HEPES, indicating reversible adsorption and desorption processes in both cases. At lower concentrations (0.5, and $1x10^{-3}$ mol/L), the phase shifts were larger with OR51E2, reaching 3.1 fold higher at $1x10^{-3}$ mol/L. On the other hand, at the highest concentration ($5x10^{-3}$ mol/L), the phase shift with OR51E2 was slightly smaller than that without OR51E2. The detection limits were $5x10^{-4}$ mol/L with OR51E2, and $1x10^{-3}$ mol/L without OR51E2. The Poynting vector for TM mode light in the Si waveguide is present in both sensing region with OR51E2 as well as sensing region without OR51E2, as illustrated in Fig. 5. Since each ND-OR binds a single molecule and the surface density of OR51E2 on the Si surface is much lower than that of SA molecules, the RI change due to molecular recognition by OR51E2 is finite. In contrast, the RI change caused by SA molecules present in the sensing region without OR51E2 is proportional to the SA concentration. We have calculated the local and bulk sensitivity, which are the phase shift divided by the local RI change averaged in the 10 nm-high region on the Si surface considering diameter of ND-ORs of about 10 nm, and bulk RI change in sensing region without OR51E2, by calculating the TM mode effective refractive index change using the refractive indices of 3.44 for Si, 1.44 for SiO_2 [25], 1.349 for HEPES buffer [26] at the

wavelength of 1300 nm, as schematically shown in Fig. 5. The calculated local and bulk sensitivities were 196 and 833 rad/RIU, respectively. For a phase shift of 0.082π rad at 1×10^{-3} mol/L SA without OR51E2, the bulk RI change is estimated as 0.082π / (196 + 833) = 2.5×10^{-4} RIU. It was reported that RI of water was 1.3324 for the 589 nm wavelength light, and 1.3225 for the 1300 nm light, showing the difference of $1x10^{-2}$ between them. Assuming the same wavelength deviation, the RI of 0.05 mol/L HEPES (1.339 at 589 nm) is ~1.349 at 1300 nm. The RI increment by $1x10^{-3}$ mol/L SA is reported as $8x10^{-4}$ RIU [27], which is the same order as the estimated bulk RI change of $2.5x10^{-4}$ RIU. The corresponding phase shift from bulk RI change in the OR-decorated Si waveguide is $2.5x10^{-4}$ RIU x 833 rad./RIU = 0.067π rad. Given the total phase shift of 0.26π rad. at $1x10^{-3}$ mol/L SA with OR51E2, the local RI change averaged over the 10 nm surface region is (0.26π - 0.067π) rad. / 196 rad./RIU = $3.1x10^{-3}$ RIU. Since the substrate surface is not fully covered with ND-ORs, the local RI change is likely to exceed the estimated value of $3.1x10^{-3}$ RIU. Since the RI difference between 4.2 mol/L SA [27] and 0.05 mol/L HEPES is $3.6x10^{-2}$, and the tested concentration here is $1x10^{-3}$ mol/L, the estimated local RI change of $3.1x10^{-3}$ is unlikely due to the concentrated SA molecules. Instead, it is likely reflects structural changes in the OR protein [9] upon the recognition of SA molecules. Figure 5 shows the schematic image of the distribution of SA molecules near the Si waveguides with and without ORs.

In conclusion, we investigated the responses of OR51E2 to SA injection on a Si MZI sensor. ND-OR immobilization was confirmed by ELIZA method. Sensitivity with OR51E2 was 3.1 times higher at $1x10^{-3}$ mol/L compared to without OR51E2. A local RI change of $3.1x10^{-3}$ RIU due to molecular recognition by OR51E2 was theoretically estimated, along with schematic molecular behavior. Integrating various ORs [8, 22] on Si MZI sensors, alongside reference MZI sensor without ORs enables selective detection of diverse odorant molecules. Sensitivity and detection limit can be further improved by extending the waveguide length and using Si rib waveguides with lower propagation loss [28-30]. Employing Si_3N_4 core layers with visible light will enhance the phase shifts from RI changes [5], reduces water-induced loss, and suppresses non-specific signals. Signal acquisition through the responses of ORs to odorant molecules in the gas phase [31, 32]—as demonstrated in the detection of biogenic volatile organic compounds [33] and acetic acid [34] for agricultural and food inspection applications—represents a key challenge in mimicking animal-like detection of diverse odorant molecules.

Acknowledgments

This work was partially supported by the JGC-Saneyoshi Scholarship Foundation(Y.F). The authors thank Dr. K. Ikebukuro for providing the termination protocol by maleimide bases of the Si surface, and Mr. J. Jiajue and Dr. R. Kawano for providing the PDMS-based μ-fluidics.

References

1) M. Aleixandre, J. Lozano, J. Gutierrez, I. Sayago, M.J. Fernandez, and M.C. Horrillo, Sensors and Actuators **B 131**, 71 (2008).
2) H. Mitsuno, T. Sakurai, S. Namiki, H. Mitsuhashi, and R. Kanzaki, Biosensors and Bioelectronics, **65**, 287 (2015).
3) G. Imamura, K. Shiba and G. Yoshikawa, Jpn. J. Appl. Phys. **55**, 110283 (2016).
4) T. Murugathas, H. Y. Zheng, D. Colbert, A. V. Kralicek, C. Carraher, and N. O. V. Plank, ACS Appl. Mater. Interfaces, **11**, 9530 (2019).
5) L. Laplatine, M. Fournier, N. Gaignebet, Y. Hou, R. Mathey, C. Herrier, J. Liu, D. Descloux, B. Gautheron, and T. Livache, Opt. Express **30**, 33955 (2022).
6) K. Minami, G. Imamura, R. Tamura, K. Shiba, and G. Yoshikawa, Biosensors **12**, 762 (2022).
7) C. Homma, M. Tsukiiwa, H. Noguchi, M. Tanaka, M. Okochi, H. Tomizawa, Y. Sugizaki, A. Isobayashi, Y. Hayamizu, Biosensors and Bioelectronics, **224**, 115047 (2023).
8) H. Kida, Y. Fukutani, J. Mainland, C. March. A. Vihani, Y. Li, Q. Chi, A. Toyama, L. Liu, M. Kameda, M. Yohda , and H. Matsunami, Nature Commun. **9**, 4556 (2018).
9) C. B. Billesbølle, C. A. de March, W. J. C. van der Velden, N. Ma, J. Tewari, C. L. del Torrent, L. Li, B. Faust, N. Vaidehi, H. Matsunami, and A. Manglik, Nature, **615**, 742 (2023).
10) H. Yang, D. Kim, J. Kim, D. Moon, H. S. Song, M. Lee, S. Hong, T. H. Park, ACS Nano **11**, 11847 (2017).
11) T. Yamada, H. Sugiura, H. Mimura, K. Kamiya, T. Osaki, and S. Takeuchi, SCIENCE ADVANCES,**7**, eabd2013 (2021).
12) T. Yoshii, I. Takayama, Y. Fukutani, T. Ikuta, K. Maehashi, and M. Yohda, Anal. Sci., **38**, 241 (2022).
13) Encyclopedia of Sensors and Biosensors, edited by R. Narayan, Elsevier, 10.1016/B978-0-12-822548-6.00099-6., ISBN: 9780128225486.
14) K. D. Vos, J. Girones, T. Claes, Y. D. Koninck, S. Popelka, E. Schacht, R. Baets, and P. Bienstman, IEEE Photonics Journal, **1** 225 (2009).
15) M. Iqbal, M. A. Gleeson, B. Spaugh, F. Tybor, W. G. Gunn, M. Hochberg, T. Baehr-Jones, R. C. Bailey, and L. C. Gunn, IEEE J. Sel. Top. Quantum Electron. **16**, 654 (2010).

16) M. K. Park, J. S. Kee, J. Y. Quah, V. Netto, J. Song, Q. Fang, E. M. L. Fosse, G-Q. Lo, Sensors and Actuators B, **176** 552 (2013).
17) R. Halir, L. Vivien, X. Le Roux, D. X. Xu, and P. Cheben, IEEE Photonics J. **5**, 6800906 (2013).
18) I. Molina-Fernandez, J. Leuermann, A. Ortega-Monux, J. Gonzalo, Wanguemert-Perez, and R. Halir, Optics express **27**, 12616, (2019).
19) R. J. J. van Gulik, B. M. de Boer, and P. J. Harmsma, IEEE J. Sel. Top. Quantum Electron., **23**, 8200207 (2017).
20) J. Leuermann, A. Fernández-Gavela, A. Torres-Cubillo, S. Postigo, A. Sánchez-Postigo, L. M. Lechuga, R. Halir, and Í. Molina-Fernández, Sensors **19**, 3671 (2019).
21) L. Laplatine, S. Messaoudene, N. Gaignebet, C. Herrier, and T. Livache, Sensors, **24**, 1712 (2024).
22) Y. Fukutani, R. Tamaki, R. Inoue, T. Koshizawa, S. Sakashita, K. Ikegami, I. Ohsawa, H. Matsunami, and M. Yohda, J. Biol. Chem. **294**, 14661 (2019).
23) https://www.cfsciences.com/products/kit/117-kit/standard-2/629-nanodisc-bd-kit (accessed on Aug. 8, 2025)
24) https://www.atto.co.jp/products/luminescence_absorption/elisa/hrpelisa/wse-7145-ezelisa-tmb (accessed on Aug. 8, 2025)
25) Refractive index database: https://refractiveindex.info/ (accessed on Aug. 1, 2025)
26) https://www.chemicalbook.com/ChemicalProductProperty_JP_CB5408557.htm (accessed on Aug. 1, 2025)
27) https://chemistry.mdma.ch/hiveboard/rhodium/pdf/chemical-data/prop_aq.pdf (accessed on Aug. 8, 2025)
28) A. Densmore, D.-X. Xu, S. Janz, P. Waldron, T. Mischki, G. Lopinski, A. Delâge, J. Lapointe, P. Cheben, B. Lamontagne, and J. H. Schmid, Optics Letters **33** 596 (2008).
29) P. Dong, W. Qian, S. Liao, H. Liang, C-C. Kung, N-N Feng, R. Shafiiha, J. Fong, D. Feng, A. V. Krishnamoorthy, and M. Asghari, Opt. Express **18**, 14474 (2010).
30) A. Brimont, X. Hu, S. Cueff, P. R. Romeo, G. S. Girons, A. Griol, A. Zanzi, P. Sanchis, and R. Orobtchouk, IEEE Photon. Tech. Lett., **28**, 299 (2016).
31) H. Deng, H. Mitsuno, R. Kanzaki, and T. Nakamoto, IEEE Sensor Journal **21** 21184 (2021).

32) R. Kanemaki, K. Kishigami, M. Saito, M. Yohda, and Y. Fukutani, Int. J. Mol. Sci. **26**, 1566 (2025).
33) H. Shimizu, R. Ogino, and M. Hasumi, Jpn. J. Appl. Phys., **64**, 050904 (2025).
34) R. Minowa, M. Hasumi, and H. Shimizu, IEEJ Trans. Electr. Electron. Eng. (under review).

Figures

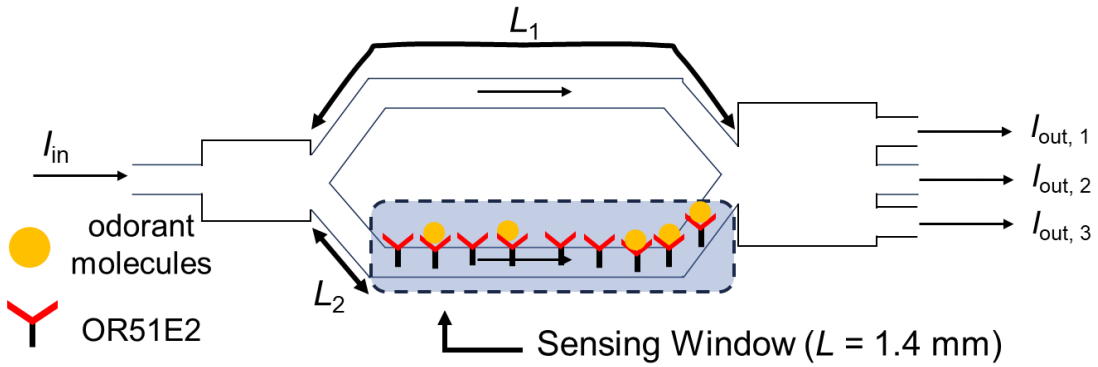

Fig. 1. Schematic illustration of Si waveguide Mach-Zehnder interferometer sensors decorated with ORs.

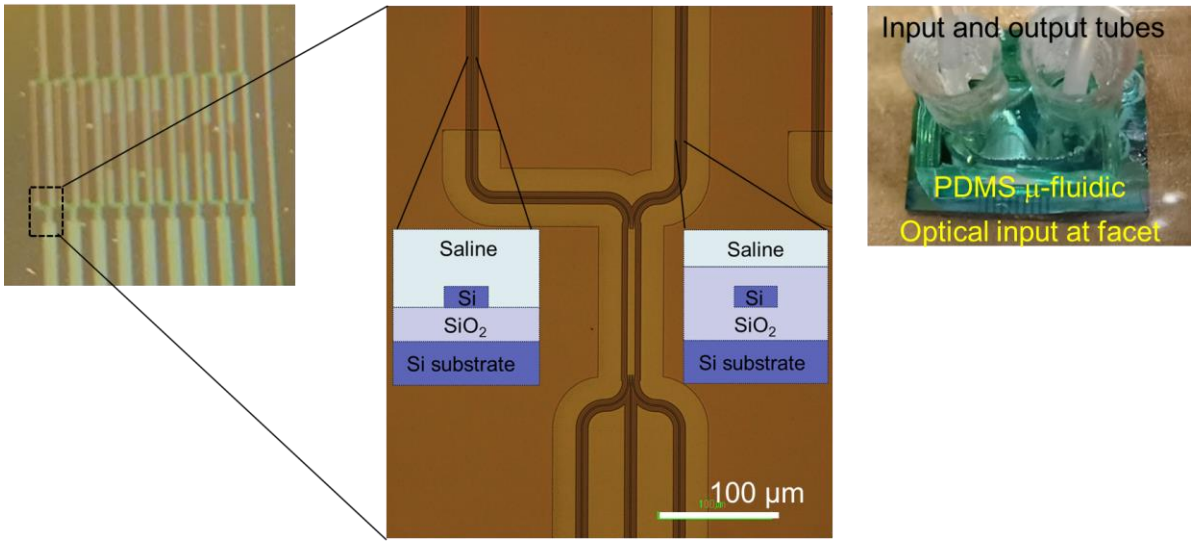

Fig. 2. Optical microscope images of Si waveguide Mach-Zehnder interferometer sensors. An inset show a die integrated with a PDMS µ-fluidic device.

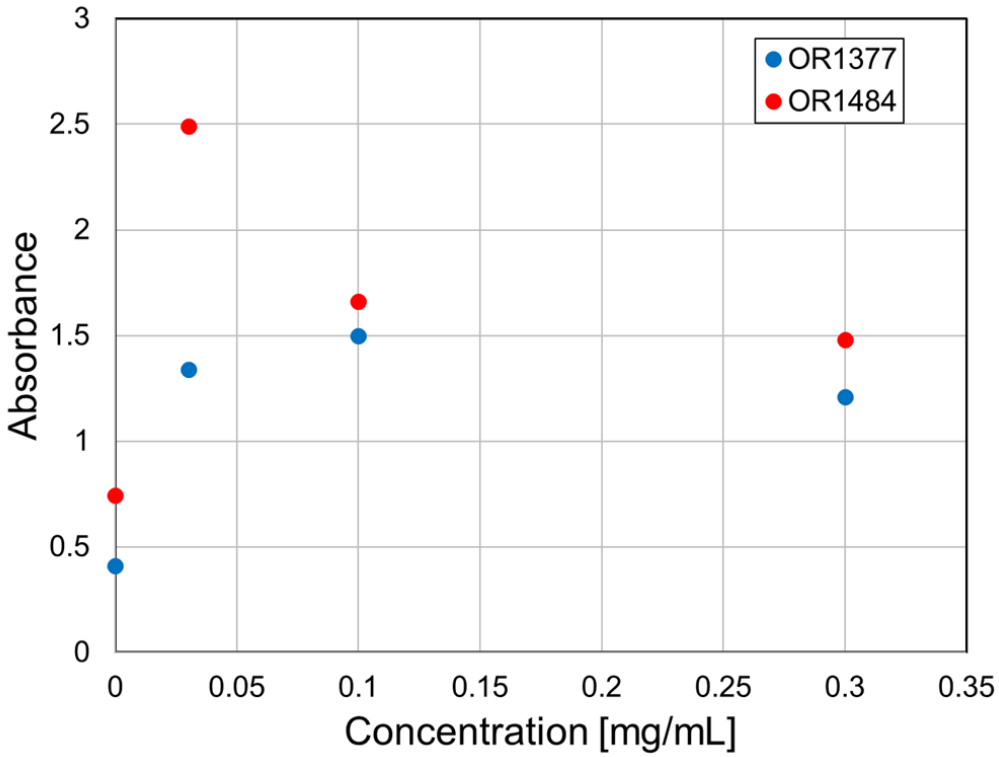

Fig. 3. Absorbance measured by ELISA method at concentrations of 0.03, 0.1, and 0.3 mg/mL for OR1377 and OR1484.

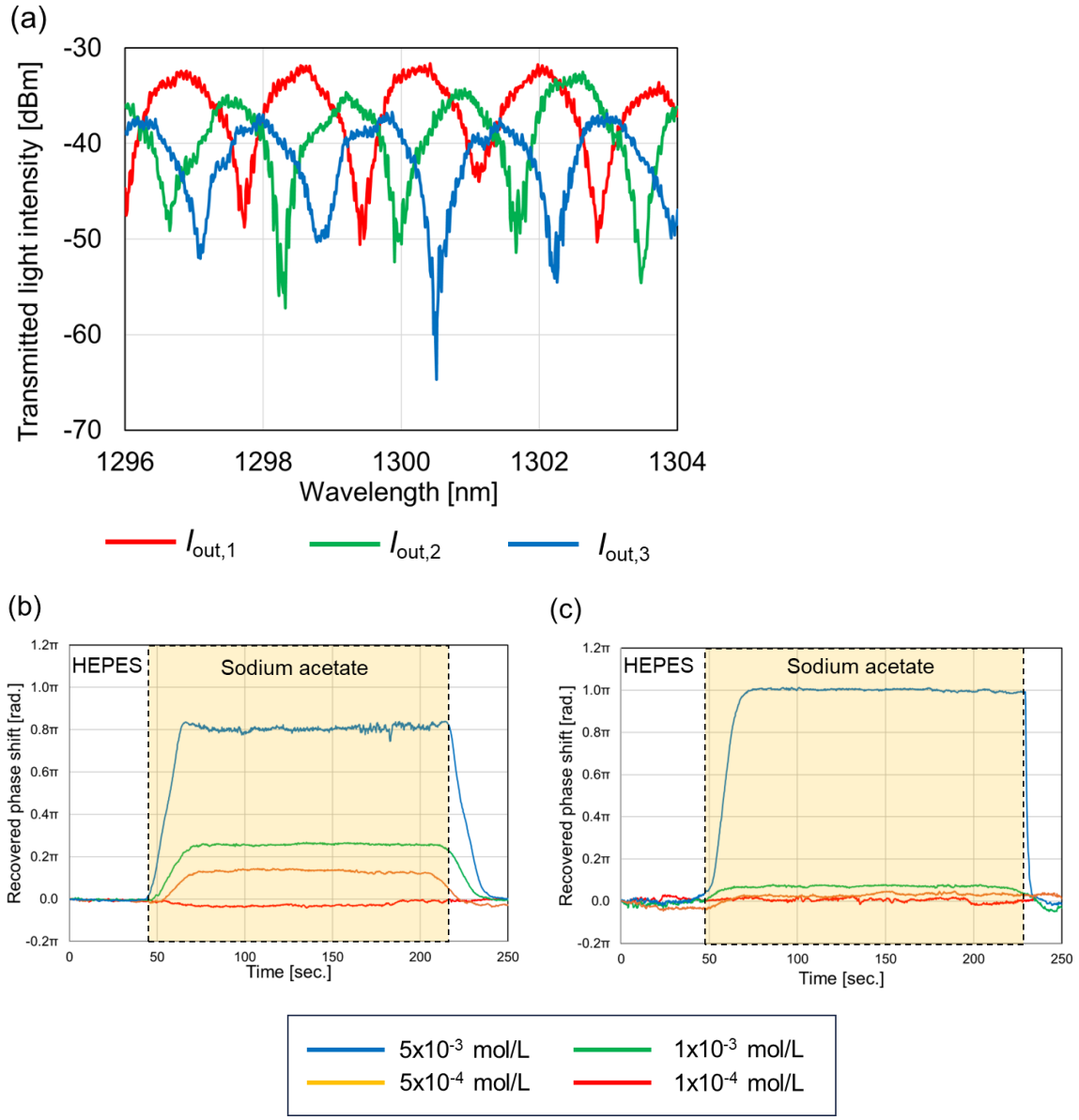

Fig. 4. (a) Wavelength dependence of transmitted light intensity of the MZI in air. Time evolution of recovered phase shift in Si-MZI sensors (b) with and (c) without OR51E2.

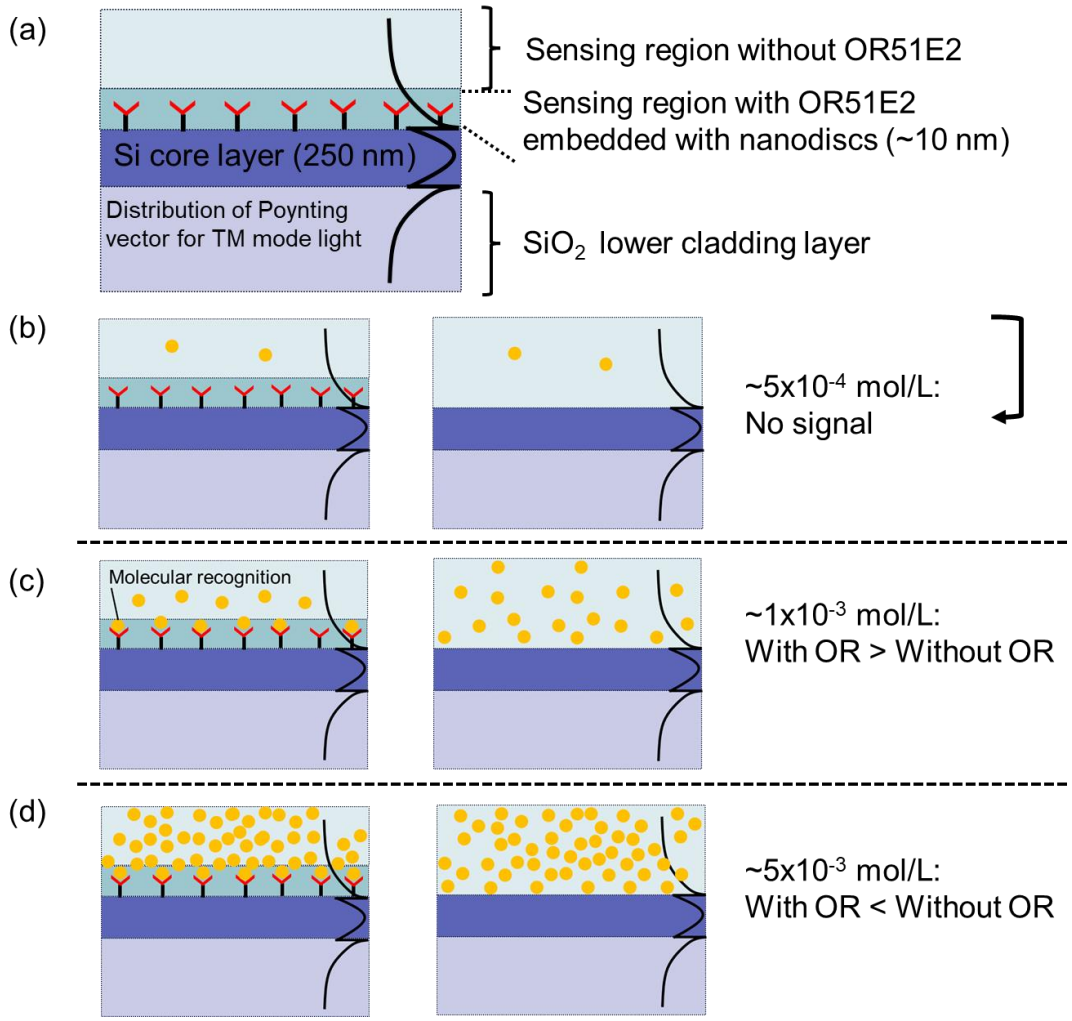

Fig. 5. Schematic illustrations of Si-MZI sensors with and without OR51E2: (a) without odorant molecules, and with odorant molecules at (b) low, (c) medium, and (d) high concentrations.